

26 I. INTRODUCTION

27 Fault weakening is a major phenomenon driving the dynamics of large earthquakes
28 because the evolution of fault friction during slip controls dynamic stress drop and heat
29 creation (Di Toro et al., 2006; Rice, 2006). A large number of physical phenomena can
30 promote fault weakening, including thermal pressurization (Wibberley and Shimamoto,
31 2005), thermal decomposition (Han et al., 2007; Sulem et al., 2009), nanopowder (Han et al.,
32 2010) or gel lubrications (Goldsby and Tullis, 2002; Di Toro et al., 2004), flash heating of
33 asperities and fault gouge melting. Recent high-velocity experiments documented these last
34 two phenomena and confirmed that flash heating at contacting asperities occurs rapidly and
35 leads to localized patches of molten rock which can eventually merge and pervasively
36 lubricate the fault (Hirose and Shimamoto, 2005, Goldsby and Tullis, 2011). According to this
37 model, the very first stage of frictional sliding can be computed by a linear mixing law
38 between undeformed (i.e. intact) and flash-heated asperities (Rice, 2006). In this model, the
39 balance between these asperity populations is controlled by the ratio of the sliding velocity to
40 a certain characteristic weakening velocity. This model was further used in a dynamic model,
41 in combination with rate-and-state friction (RSF) laws (Bizzari, 2009). It also showed good
42 agreement with the experimental results reported in Goldsby et al. (2011), although the
43 observed scenario implied the creation of a gouge layer (of a few tens of micrometers) during
44 fault weakening. The authors then discussed the possibility that distributed deformation (i.e.
45 shearing) in a sufficiently thick gouge layer might prevent melting. However, further
46 experiments performed in the presence of a thick gouge layer showed that weakening occurs
47 in that case too. Sone and Shimamoto (2009) reported slip localization in a thin section of a
48 millimetric gouge layer but no pervasive interface melting, while Reches et al. (2010)
49 reported spontaneous formation and thickening of a gouge layer and the development of
50 glassy patches (i.e. solidified melt).

51 Recent triaxial laboratory earthquake experiments illuminated that flash heating and
52 frictional melting can be observed even on experimental faults experimenting stick-slip events
53 (Aubry et al., 2018; Aubry et al., 2020). In these experiments performed at confining
54 pressures much larger than those used in high-velocity shearing experiments, pervasive
55 melting of the interface was always accompanied by the observation of a thin (i.e. a few μm -
56 thick) layer of fault gouge. The detailed succession of events leading the sliding surfaces to
57 evolve to that particular stage was however unavailable to the experimental device. In the case
58 of pervasive interface melting, the friction dependence on normal stress and sliding velocity
59 has been formulated (Nielsen et al., 2008). Unfortunately, this model does not cover the
60 complex transient mechanisms leading to pervasive melting of the interface. Complex
61 interactions between the granular gouge and the molten rock are indeed expected during this
62 weakening stage, that cannot be easily accounted for in a simple theoretical model.

63 To solve this issue, we document granular simulations during which thermo-
64 mechanical phenomena occur on faults during seismic events. We consider that a certain layer
65 of fault gouge pre-exists in the interface, or at least that it is created by surface abrasion and
66 grains comminution in the very early stages of sliding, prior to the occurrence of melting. We
67 focus on the granular behaviour of the deformed gouge, since this behaviour is expected to
68 promote shear localization. A particular attention is put on the thermal effects related to (i)
69 heat creation at the frictional contacts between gouge grains, (ii) heat diffusion through
70 contacts between such grains, and (iii) heat diffusion in the medium surrounding the fault. We
71 then explore the influence of progressive melting of the gouge on the accommodation mode
72 within the interface, and on its consequences on fault friction and rheology.

73

74

75

76 II. GRANULAR SIMULATION OF FAULT GOUGE

77 *a. Numerical model*

78 Discrete Element Modelling (DEM, Cundall and Strack, 1979) is a powerful simulation
79 approach which represents a granular assembly as an explicit collection of rigid bodies,
80 submitted to Newtonian dynamics and to user-defined interaction models. It has become very
81 common in a number of scientific fields where the simulation of granular systems are of
82 practical or academic interest. Numerical tribology makes an extensive use of this technique
83 to simulate the rheology of tribological third bodies (i.e. discontinuous layers of material
84 trapped in a contact, originating from damage of contacting surfaces (Iordanoff et al., 2005,
85 Renouf et al., 2011, Mollon, 2015), and controlling frictional behaviour). As a straightforward
86 extension of this concept, geophysicists have employed the same approach to simulate fault
87 gouge in sliding seismic faults (Guo and Morgan, 2007). In this section, we stick to this
88 classical framework by considering a purely granular fault gouge. As will be elaborated in
89 Section IV, this framework will have to be enriched to properly represent partial melting, but
90 it is a good starting point to analyse the initial behaviour of the fault before the first
91 appearance of melt.

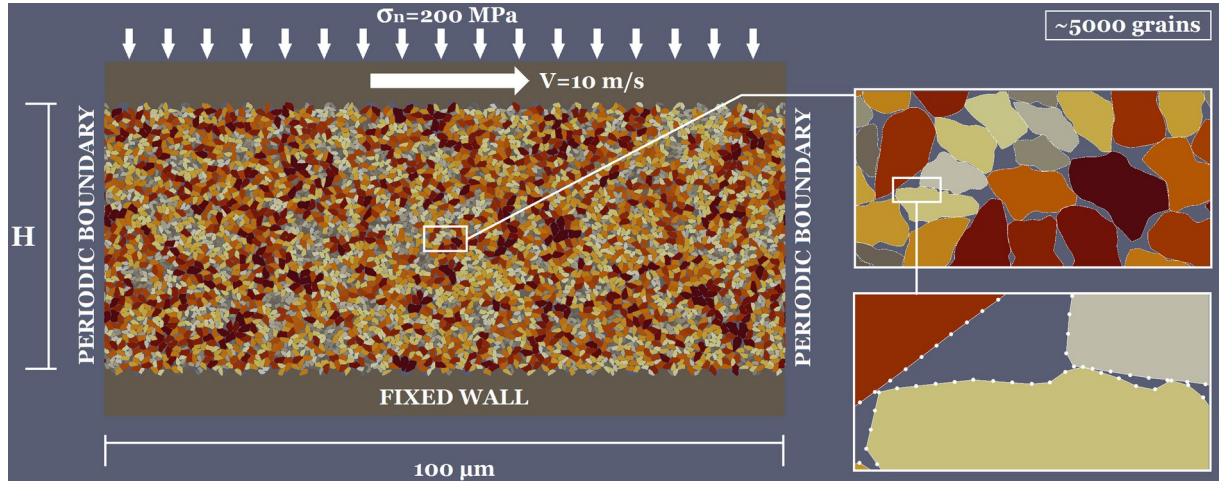
92

93 As shown in Figure 1, we consider a purely granular fault gouge composed of a few
94 thousands of grains, generated with the package Packing2D (Mollon and Zhao, 2012). Their
95 shapes are randomly and fractally generated. In the present case, the generation tool is
96 calibrated to provide angular and faceted grains typical of comminuted gouges (Figure 1).
97 The particle size distribution is uniform, with a median particle diameter of 1 μm and a ratio
98 of 2 between the smallest and the largest particle sizes. This distribution is rather narrow
99 when compared to the fractal distributions typically encountered in the field (Muto et al.,
100 2015), but it allows to run simulations in a reasonable amount of time while ensuring a

101 sufficient model size. This sample is closely packed by the generation tool in a rectangle with
102 a length L and a height H_{gen} . It is then introduced in the simulation software MELODY2D
103 (Mollon, 2018). This code is able to deal with such complex particle shapes by employing a
104 robust two-pass node-to-segment contact algorithm. Each grain contour is thus discretized by
105 approximately 50-100 nodes and the same number of segments. This feature provides an
106 additional level of complexity when compared to traditional DEM simulating circular or
107 spherical grains, and consistently improves the quality of the granular simulations, especially
108 regarding shear localization (Mollon et al., 2020).

109 The sample is positioned between two horizontal walls with a sinusoidal roughness
110 designed to avoid wall-slip effects since grain accommodation within the gouge is our
111 primary interest. Periodic boundary conditions are applied on the two lateral faces of the
112 sample, allowing deformation at large slips. The lower wall is fixed in displacement, while the
113 upper wall is applied a vertical downward stress of 200 MPa to simulate confining pressure at
114 typical seismogenic depths. During the compaction stage, the contact model between the
115 grains is frictionless in order to maximize the compacity of the sample up to a volume fraction
116 of 0.86, with a corresponding gouge thickness H . Volume fraction refer in this paper to the
117 proportion of the apparent volume of the gouge occupied by solid or liquid matter (but not
118 gaseous). After compaction, grains contacts are driven by a frictional model without cohesion
119 (Mohr-Coulomb type, friction coefficient of 0.8). This large value follows the
120 recommendations of Mollon et al. (2020) and aims to compensate the smoothing of the grains
121 surfaces during their discretization. The upper wall is submitted to a horizontal velocity of 10
122 m/s (i.e., a velocity higher than typical sliding velocities in earthquakes in order to accelerate
123 the simulation process), while its vertical motion is set free in order to accommodate possible
124 dilation or compaction in the sheared gouge. The inertial number (MiDi, 2004) of the granular
125 system in the model is close to $9e^{-4}$, which classifies it in the category of “dense quasi-static

126 shear flows” (Forterre and Pouliquen, 2008). This means that the inertial forces are negligible
 127 and that shear rate has no significant effect on the grains kinematics.
 128



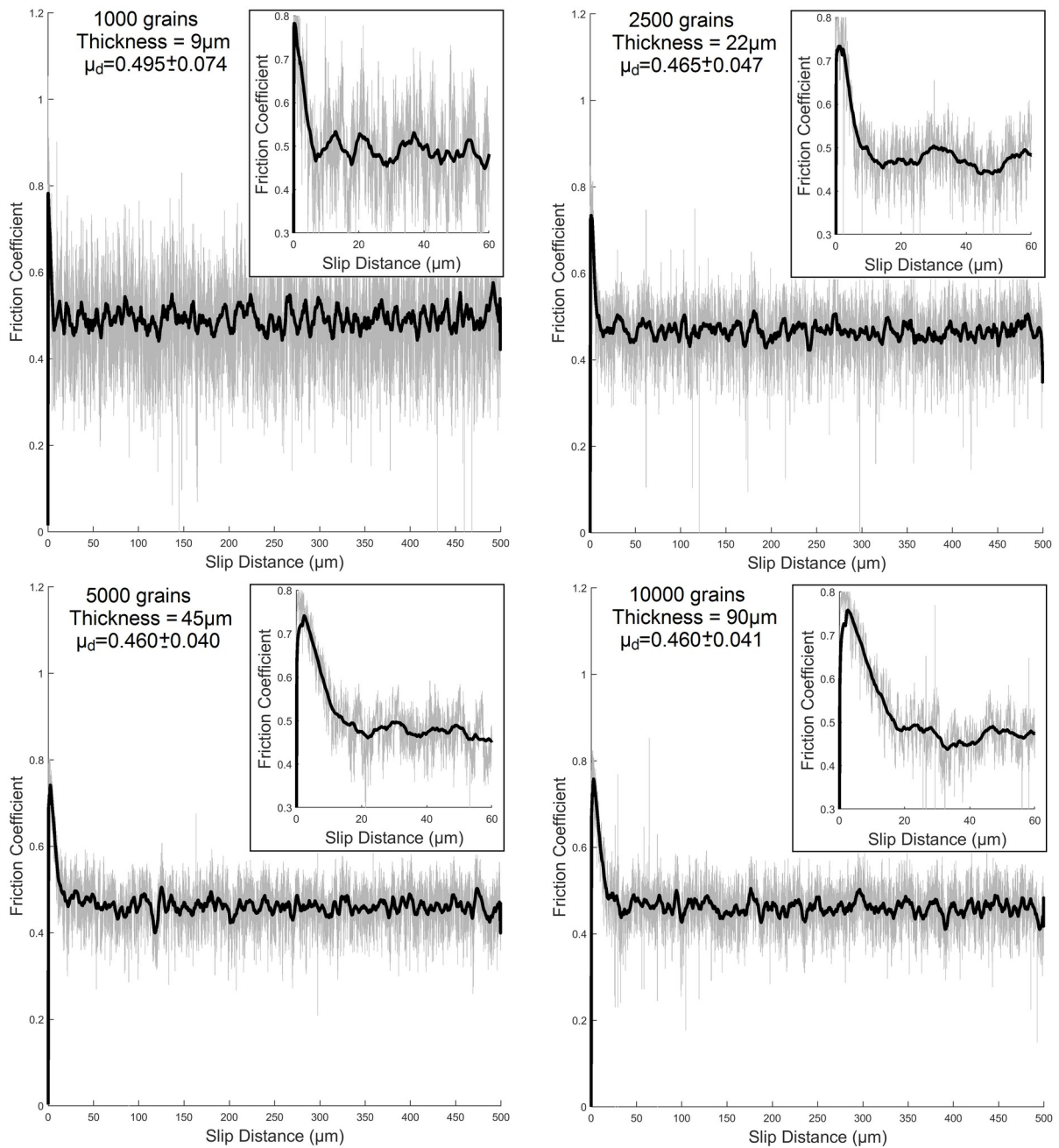
129
 130 *Fig.1. Sketch of the model for a dry granular gouge; Upper insert: detailed view of grains*
 131 *morphologies; Lower insert: zoom on grains nodes and segments used by the contact algorithm.*

132

133 ***b. Influence of the dimensions of the gouge layer***

134 In order to determine the size of the representative volume element (RVE), several values
 135 of the model length L are first tested, ranging from 20 μm to 200 μm , with a constant
 136 thickness H of about 45 μm . Below the optimal model length $L=100 \mu\text{m}$, the friction
 137 coefficient (defined as a ratio of shear stress and normal stress) strongly fluctuates along
 138 simulated time, indicating that the system is too small to be statistically reliable. Hence, the
 139 model length is kept constant and equal to 100 μm .

140



141

142 *Fig.2. Friction coefficients as functions of sliding distance for four different gouge thicknesses; grey*
 143 *lines: raw numerical data; bold black lines: moving average; Inserts: first 60 μm of slip*

144

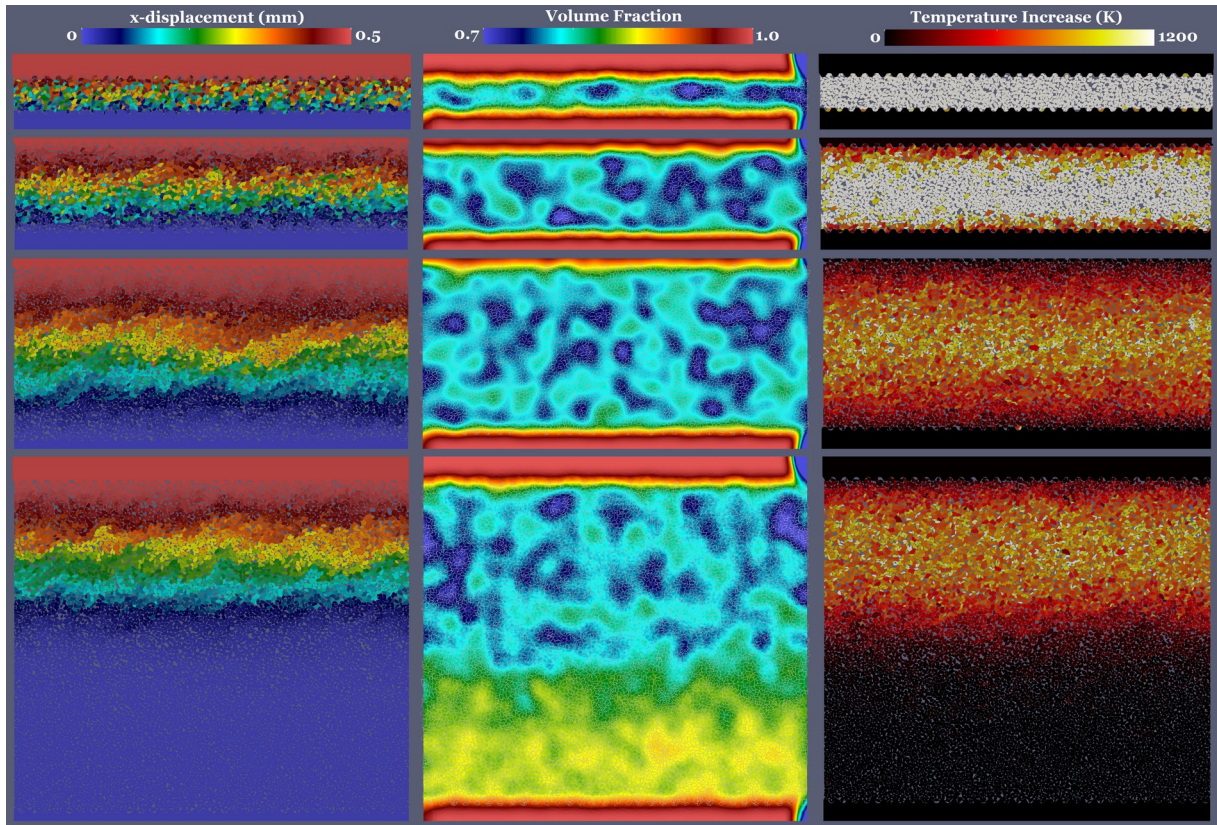
145 Four gouge models are built with compacted thicknesses of 9, 22, 45, and 90 μm ,
 146 containing respectively 1000, 2500, 5000 and 10000 grains. The time-series of the friction
 147 coefficients obtained for these four cases are provided in Fig.2. All these simulations show
 148 that sliding first induces a strong friction peak of 0.75-0.8, followed by a linear slip-
 149 weakening of the fault, and by a friction plateau where a frictional steady-state has been

150 reached. This initial peak is related to the energy needed by the sample to dilate (i.e. break the
151 initial compacted configuration of the grains) and reach a lower density at which shearing is
152 possible. The weakening part is very short for the less thick gouge, but gets more delayed
153 when the thickness increases. The cases $H=45\ \mu\text{m}$ and $H=90\ \mu\text{m}$ exhibit similar weakening
154 behaviours.

155

156 *c. Steady state friction and kinematics*

157 Since we are interested in fault weakening induced by partial melting, we disregard any
158 transient phenomenon related to the very onset of sliding, and focus on the steady state
159 behaviour of the simulations. Indeed, the melt-related weakening is a delayed phenomenon,
160 which occurs after a sliding distance that is much larger than that concerned with the initial
161 dilation. In the steady state, the average friction of the dry (i.e. not melted) gouge μ_d is only
162 moderately influenced by the model thickness: it is equal to 0.495 for the $9\ \mu\text{m}$ -thick fault,
163 and stabilizes at 0.460 for thicknesses equal to or larger than $45\ \mu\text{m}$. Thicker faults also tend
164 to stabilize the evolution of the friction coefficient and to reduce its fluctuations.

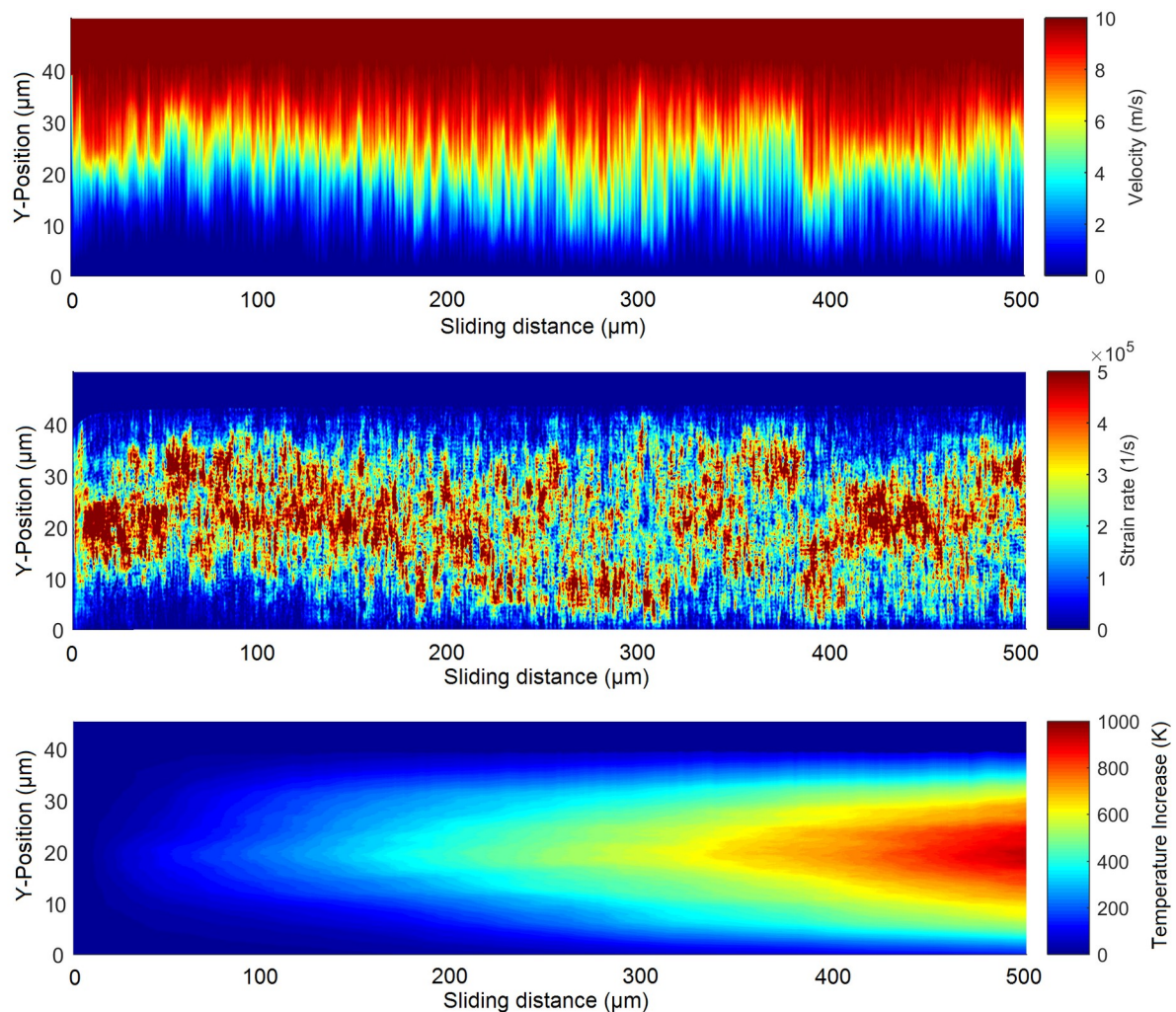


165

166 *Fig.3. Views of the models with four different gouge thicknesses ($H=9, 22, 45,$ and $90 \mu\text{m}$, from top to*
 167 *bottom) after $500 \mu\text{m}$ of sliding. Left: Final Horizontal Displacement; Middle: Final Volume*
 168 *Fraction; Right: Final Temperature Increase in adiabatic conditions*
 169

170 However, it appears that most of the slip is accommodated in the central part of the layer in
 171 the $45 \mu\text{m}$ -thick case, and that some areas close to the walls remain almost undisturbed. This
 172 phenomenon is even more present in the $90 \mu\text{m}$ -thick case, where more than one half of the
 173 gouge thickness remains undeformed during shearing. In the $90 \mu\text{m}$ -thick case, the sample
 174 only dilates in the upper part accommodating shearing and reaches an average volume
 175 fraction of 0.77 in the shear band: no shear takes place in the lower part as the sample is still
 176 in its initial state of compaction (i.e., volume fraction about 0.86). From this calibration, we
 177 conclude that the shear localization thickness of the granular medium is close to $40 \mu\text{m}$, in
 178 good agreement with numerical and experimental estimates which usually range between 15
 179 and 50 times the median grain size (Torsedillas et al., 2004; Mollon et al, 2020). Thus, all the
 180 remaining simulations described in this paper will adopt an initial gouge thickness of $45\mu\text{m}$.

181 A more detailed view of the accommodation mechanism is provided in Figure 4 for the 45
 182 μm -thick sample. Key local quantities are averaged along the horizontal direction in order to
 183 extract instantaneous vertical profiles. The figure shows that local shear rate keeps a rather
 184 constant maximum value (close to $5 \cdot 10^5 \text{ s}^{-1}$) but that the locus of this maximum evolves in
 185 time. Hence, the instantaneous shearing profile is very sharp (at a given time, most of the
 186 shearing occurs on a thickness smaller than $10 \mu\text{m}$). The idea of active sites shifting rapidly
 187 within a broader zone postulated in Rice (2006) is thus confirmed by our numerical results.



188
 189 *Fig.4. Evolution of the vertical profiles of key quantities (averaged in the horizontal direction) for the*
 190 *reference model during 500 μm of sliding; Top: Horizontal Velocity; Middle: Shear Rate; Bottom;*
 191 *Temperature Increase in adiabatic conditions*
 192
 193

194 **III. THERMAL ASPECTS**

195 *a. Adiabatic temperature increase*

196 Simulating fault gouge melting requires a temperature field within the gouge and the
197 surrounding rock. A first step to achieve this issue was to implement a temperature tracker in
198 MELODY to evaluate the quantity of heat produced by frictional processes between the
199 grains during shearing. The tracker records mechanical energy dissipation phenomena on
200 contacting grains and transforms the energy into heat (disregarding any other heat sink such
201 as local physico-chemistry). Each grain in a contacting and sliding pair receives a temperature
202 increment:

$$\Delta T = \frac{0.8 v F \cdot \Delta t}{2} m c_p \quad (1)$$

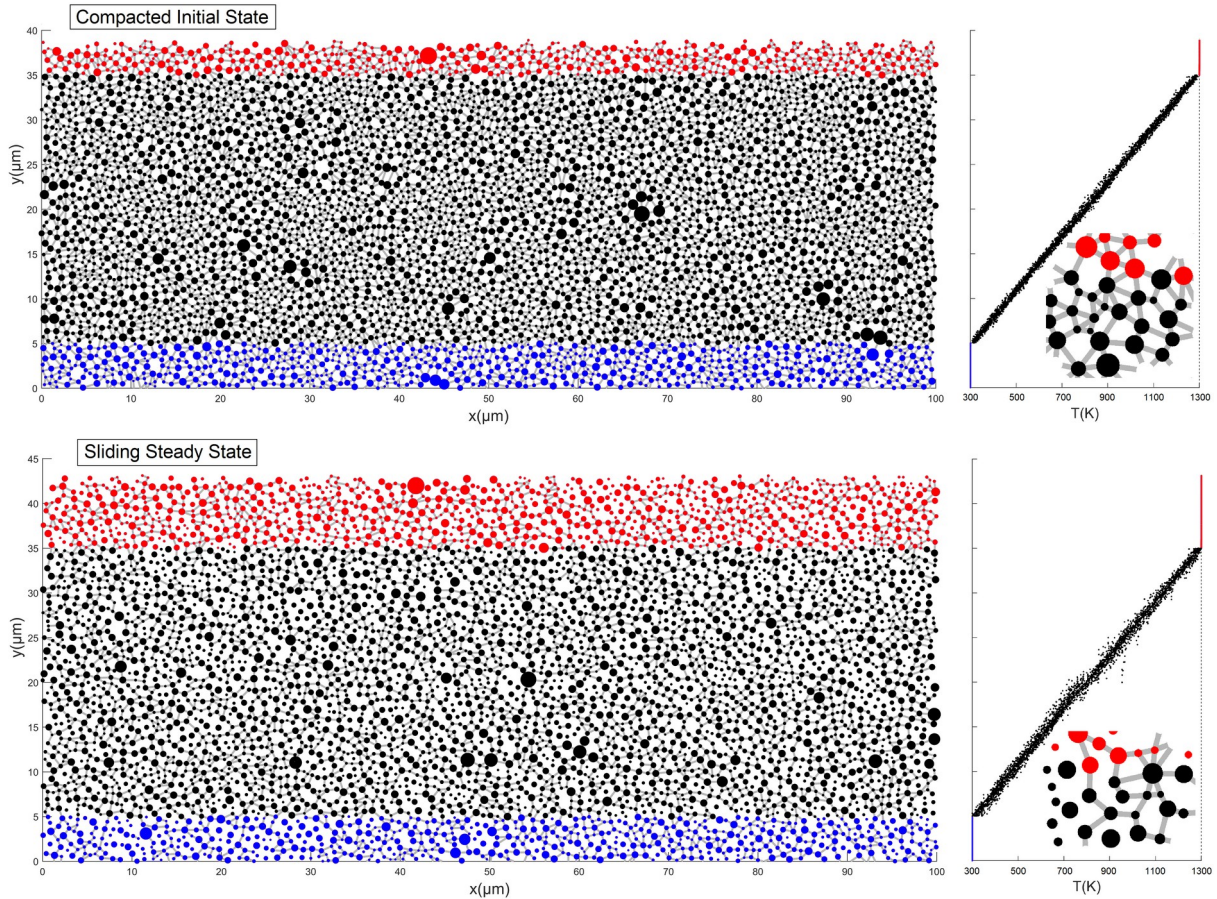
203 where Δt is the time step duration; v is the grains pair sliding velocity; F is the normal load
204 transmitted through the contact; m is the grain mass; c_p is material heat capacity; and 0.8 is
205 the interparticle friction coefficient. The field of temperature in the grains is considered as
206 homogeneous. Figure 3 shows that heat creation is restricted to the areas where shearing takes
207 place, and that higher temperatures are reached after a given sliding distance if the gouge
208 layer is thinner. Hence, temperature increase is intimately related with shear localization. Heat
209 creation is distributed over the whole thickness of the sheared layer, but is maximum in its
210 center.

211

212 *b. Contact conductivity calibration*

213 Heat creation is very heterogeneous in the grains of the sample: under these assumptions,
214 very close grains can have very different temperatures, which does not seem right (Figure 3).
215 Since mechanical contacts exist between touching grains, we shall expect a certain amount of
216 heat diffusion through them. The problem of heat flux through mechanical contacts has been
217 investigated in several studies (Madhusudana and Ling, 1995). However, in the present case,

218 the contact configurations are both complex (because of the angularity of the grains) and
 219 simplified (because of their limited discretization). Hence, we use a constant thermal
 220 conductivity k_c for all the intergranular contacts, whatever their geometry and supported load.
 221



222
 223 *Fig.5. Calibration of intergranular contact thermal conductivity under a stabilized vertical heat flux.*
 224 *Left-hand panel: Thermal network (size of the dots indicates the mass of each grain, grey lines*
 225 *indicate heat-conducting mechanical contacts, red dots (above $y=35\mu\text{m}$) are grains set at a constant*
 226 *temperature of 1300 K, blue dots (below $y=5\mu\text{m}$) are grains set at 300 K, and black dots are grains*
 227 *which remain free to evolve to their equilibrium temperature); Right-hand panel: Temperature*
 228 *profiles at thermal equilibrium and zoom on a local area of the thermal network; Top: initial*
 229 *compacted state; Bottom: after 500 μm of sliding (gouge thickness increased because of granular*
 230 *dilatancy, since thermal expansion of grains is disregarded)*
 231

232 To calibrate this conductivity, a thermal network based on the initial compacted state
 233 of the granular sample is built. We consider each grain as a node (defined by its mass and its
 234 heat capacity), and each contact as a link between two nodes. A detailed view of this network

235 is provided in Figure 5. A given node i has a temperature T_i , and the heat flux through the
236 contact between any two contacting nodes i and j is given by:

$$q_{i \rightarrow j} = k_c \cdot (T_j - T_i) \quad (2)$$

237 The term k_c in this equation is a 1D contact conductivity (unit W.K^{-1}) which provides
238 the heat flux through a given mechanical contact (if it exists), and should not be confused with
239 bulk contact conductivity of a given medium (unit $\text{W m}^{-1} \text{K}^{-1}$). To establish a general vertical
240 heat flux within the thermal network, we impose a global temperature gradient of 1000 K over
241 a thickness of 30 μm (Figure 5). Some nodes (black dots in Fig.5) are let free to adopt their
242 equilibrium temperature. This equilibrium is reached by using a simple heat diffusion
243 numerical scheme based on Eq. (2), after a relaxation time of 1 ms. The equilibrium
244 temperature field is close to a linear temperature profile (Figure 5). Assuming $k_c=1 \text{ W K}^{-1}$, we
245 obtain after relaxation a constant total heat flux (integrated on all the contacts between black
246 and blue areas, Fig. 5) of $5.969 \cdot 10^7 \text{ W/m}^2$. Under the imposed gradient of temperature, this
247 leads to a macroscopic thermal conductivity of $1.7908 \text{ W m}^{-1} \text{K}^{-1}$. For bulk Westerly granite
248 (about $2.9 \text{ Wm}^{-1}\text{K}^{-1}$), we obtain a calibrated contact conductivity of 1.6194 W K^{-1} . However,
249 thermal diffusivity reported in Vosteen and Schellschmidt (2003) for intact gouge are close to
250 $0.7 \cdot 10^{-6} \text{ m}^2\text{s}^{-1}$, which is smaller than typical values of about $1 \cdot 10^{-6} \text{ m}^2 \text{ s}^{-1}$ for bulk granite
251 (Passelègue et al., 2016; Aubry et al., 2018). We thus apply a factor 0.7 and choose a contact
252 conductivity $k_c=1.1336 \text{ W K}^{-1}$. Since this calibration relies on a homogeneous temperature in
253 each grain, it is acceptable to consider that k_c also includes a simplified heat diffusion within
254 each grain. After 500 μm of sliding, the heat flux obtained with this contact conductivity is
255 close to 0.39 times that of the initial state (Figure 5). This means that the dilation and loss of
256 many contacts induced by the shearing lower the overall thermal conductivity of the gouge
257 layer by a factor 2.5, which is considerable.

258

259 *c. Heat diffusion and temperature variability*

260 A one-dimensional thermal network on each of the vertical boundaries (with appropriate
261 conductivities and heat capacities based on bulk granite) is added to allow heat diffusion in
262 the medium surrounding the fault (Figure 6). A second pass is done on the mechanical data
263 stored at the end of the granular simulations. After setting the initial temperature of all the
264 bodies to 300 K, this second pass accounts, at each time step, for the evolving contact network
265 within the gouge (and between the grains and the walls) as described in section IIIb, and for
266 the created thermal energy obtained following the method described in section IIIa.
267 Obviously, it is not possible to record on hard drive the contact network at each time step of
268 the mechanical simulations. This approach remains however correct thanks to a sufficient
269 network sampling rate, and thanks to the fact that we are dealing with a dense quasi-static
270 flow. In contrast with a collisional granular flow, the typical contact life-time is rather long
271 and interpolation is licit. A major interest of this approach is that we can simulate several
272 sliding velocities from the same initial granular simulation. Since the flow is quasi-static (i.e.
273 near mechanical equilibrium at any time of the simulation), the time considered in the
274 granular simulation is not physical, and is just an evolution parameter. When applying the
275 heat diffusion as a second pass, it is therefore possible to modify the physical time without
276 running the granular simulation again.

277

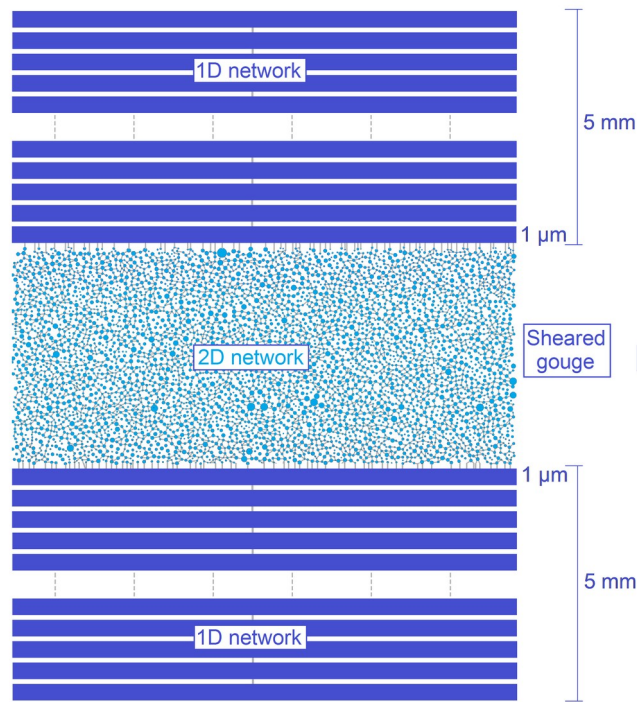


Fig.6. Mixed 1D-2D thermal network for the transient heat diffusion simulation

278

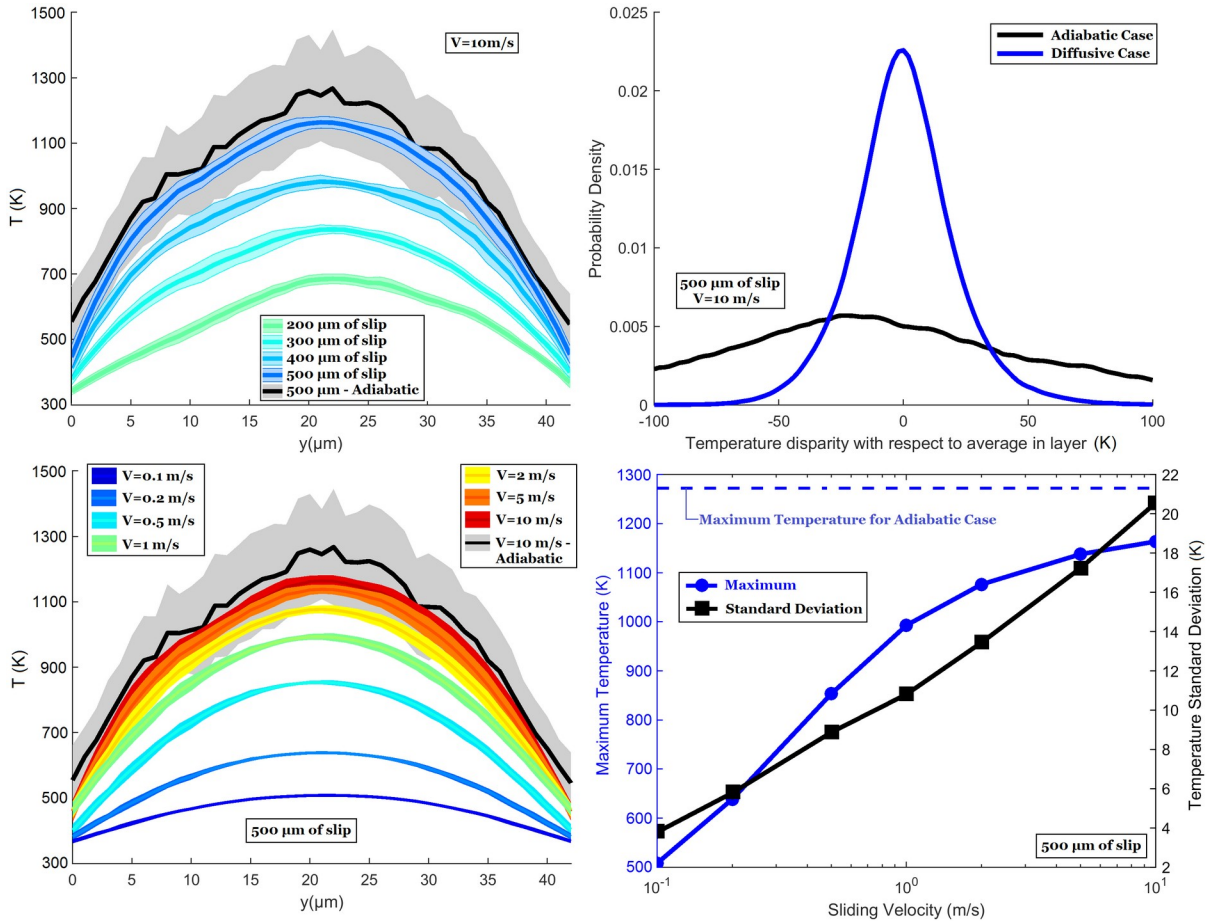
279

280

281 The results of the simulations are summarized in Figure 7. For a sliding velocity of 10 ms^{-1}
 282 (upper-left panel), a progressive temperature increase, with a maximum value close to the
 283 center of the gouge layer is observed. The diffusive case leads to a profile with a lower
 284 maximum value and a much lower variability. Temperature profiles across the gouge
 285 thickness after $500 \mu\text{m}$ of sliding for sliding velocities ranging from 0.1 m s^{-1} to 10 m s^{-1} are
 286 shown in Figure 7 (lower-left panel). Since the heat created is purely proportional to the
 287 sliding distance (and not to sliding velocity), the only difference between these cases is the
 288 time allowed for heat diffusion. It demonstrates that sliding velocity has a considerable
 289 influence on the temperature profile in the gouge layer, with maximum values ranging from
 290 500 K to 1150 K at the end of the simulation (1250 K in adiabatic conditions).

291 In order to quantify the variability of the grains temperatures, temperature statistical
 292 distributions (corrected by the average temperature in the horizontal layer for each grain) after
 293 $500 \mu\text{m}$ of sliding, are calculated both for the adiabatic and diffusive cases (Figure 7, upper-

294 right panel). The distribution for the adiabatic situation is slightly skewed and is very broad,
 295 while that of the diffusive case is quasi-gaussian and much narrower. The standard deviation
 296 obtained from this distribution ranges from 4 K in the case of low sliding velocities to 18 K
 297 for fast sliding. It is thus evident that large sliding velocities can promote larger temperature
 298 heterogeneities within the sample, largely influencing the onset of melting.



299
 300 *Fig.7. Thermal results. Upper-left: temperature profiles across the gouge thickness (\pm one standard*
 301 *deviation) at several sliding distances, for a sliding velocity of 10 ms^{-1} (adiabatic case in grey);*
 302 *Lower-left: temperature profiles across the gouge thickness (\pm one standard deviation) after $500 \mu\text{m}$*
 303 *of sliding, for different sliding velocities (adiabatic case in grey); Upper-right: Statistical distributions*
 304 *of the grains temperatures (corrected by the average temperature in their horizontal layer) in the*
 305 *adiabatic and diffusive cases; Lower-right: Maximum value and standard deviation (with respect to*
 306 *the average in horizontal layer) of the grains temperatures at different sliding velocities.*

307

308

309

310 IV. GRANULAR SIMULATION OF FAULT GOUGE MELTING

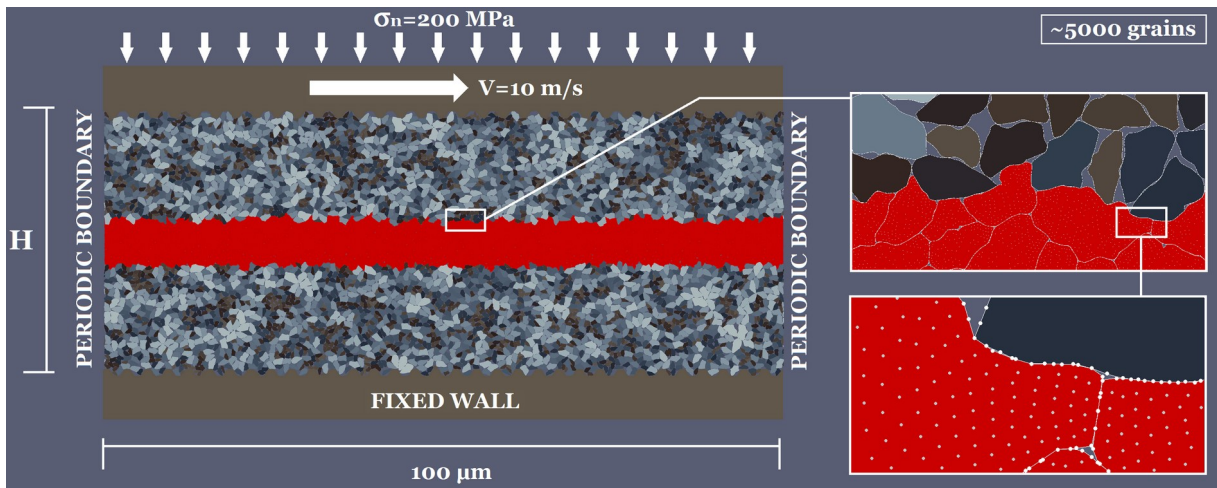
311 *a. Model description*

312 Knowing the melting point of the minerals composing the simulated gouge, it is possible
313 to predict the time and location of first appearance of rock melt in the gouge layer. From that
314 point, however, the previous results are useless because the presence of molten rock is
315 expected to considerably modify the local rheology of the gouge, altering its frictional
316 behavior and thus the amount of heat production. To go beyond that point, it is thus necessary
317 to explicitly simulate the presence of melt in granular simulations. The particular case of
318 melting in fault gouge is complex to model since, (i) the gouge layer is a ternary combination
319 of solid rock, molten rock and porosity (Aubry et al., 2018), (ii) the melt fraction can take
320 very different values (from a little melt in the granular assembly to a few solid grains inside a
321 liquid layer), (iii) this fraction evolves in space and time depending on the temperature
322 distribution, and (iv) the shear rate is very high.

323 Here, the molten grains are modelled as highly compliant, visco-elastic, frictionless,
324 incompressible bodies. This approximation retains a large part of the physics of the problem
325 (the soft, viscous and incompressible character of the melt) and provides an approximate
326 model of the local lubrication brought by the molten rock into the initially granular gouge.
327 MELODY simulates such compliant bodies using a multibody meshfree approach (Mollon
328 2018). Each body is discretized by a large number of field nodes which carry the degrees of
329 freedom in displacement. The equations of continuum mechanics extended to finite strains are
330 then solved on each grain using a weak-form. The deformed bodies can interact with each
331 other, using the contact algorithm described in Section II. The overall dynamic simulation is
332 solved in time by an explicit solver, just as in classical DEM. This approach was already
333 successfully applied in tribology and in granular physics (Mollon 2019).

334

335 In the case of solid grains, heat creation is estimated by transforming all the
 336 mechanical energy by intergranular frictional contacts into heat (Eq. (1)). However, soft and
 337 melted grains are frictionless and do not dissipate energy at their boundaries. For these
 338 particular grains, all the energy dissipation is provided by the viscous part of the constitutive
 339 law implemented in each grain. Hence, to evaluate heat creation while ensuring energy
 340 conservation in each soft grain, we simply transform all the mechanical energy dissipated by
 341 viscosity into heat.
 342



343
 344 *Fig.8. Sketch of the model for a granular gouge with partial melting (completely melted central layer*
 345 *in this case, molten grains in red); Upper insert: detailed view of grains morphologies; Lower insert:*
 346 *zoom on grains field nodes, and on nodes and segments used by the contact algorithm.*

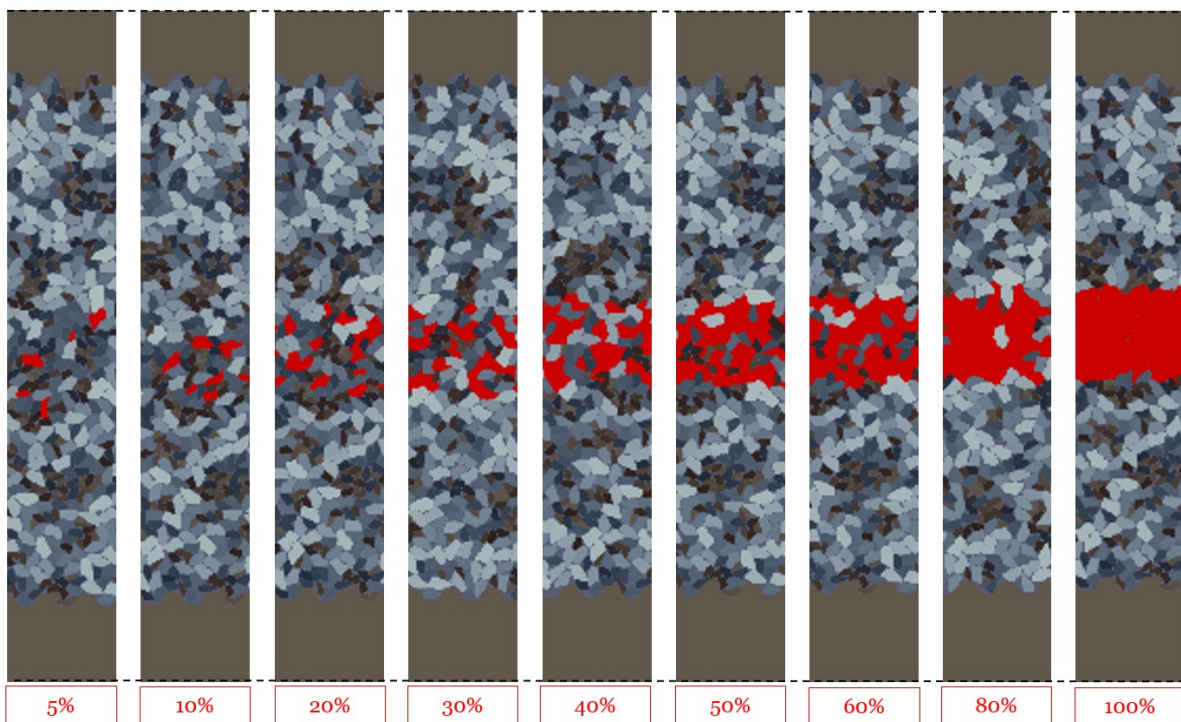
347
 348 A typical model is shown in Figure 8. In that specific case, we consider complete melting
 349 (i.e. a melt proportion $\phi_m = 1$) in a central layer of thickness $H_m \approx 8 \mu\text{m}$. The simulation process
 350 is identical to that of Section II (i.e. compaction under 200 MPa, stabilization, and shearing at
 351 a sliding velocity of 10 ms^{-1}). This simulation shows that the porosity is almost reduced to
 352 zero in the molten layer, because the soft grains deform immediately under the confining
 353 stress, while remaining quasi-incompressible. This is made possible by the relative motion of
 354 the field nodes within each body (Figure 8, lower-insert).

355

356 ***b. Influence of the melt fraction***

357 As the first molten grains seem to appear in the central area of the gouge layer, a
358 numerical campaign with a constant melt layer thickness but a varying melt proportion within
359 this layer is performed in order to cover the whole range of rheologies of the gouge layer
360 (Figure 9). This choice is made because the thermo-mechanical results of Section III (Fig. 7)
361 indicate that the first molten grains will likely appear in the central area of the gouge layer.
362 The onset of melting will thus involve interactions between a partially molten layer in the
363 center and dry granular layers around it.

364



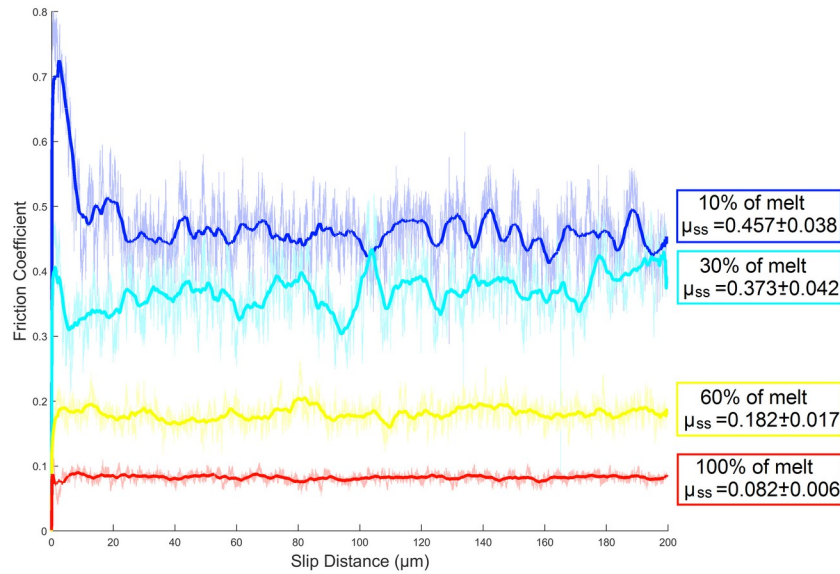
365

366 *Fig.9. Illustrative vertical slices of the simulations performed with a varying melt proportion Φ_m from*
367 *5% to 100%.*

368

369 Time series of the friction coefficients obtained for four different proportions of melt in the
370 central layer (10%, 30%; 60% 100%) are shown in Figure 10. The progressive increase of the

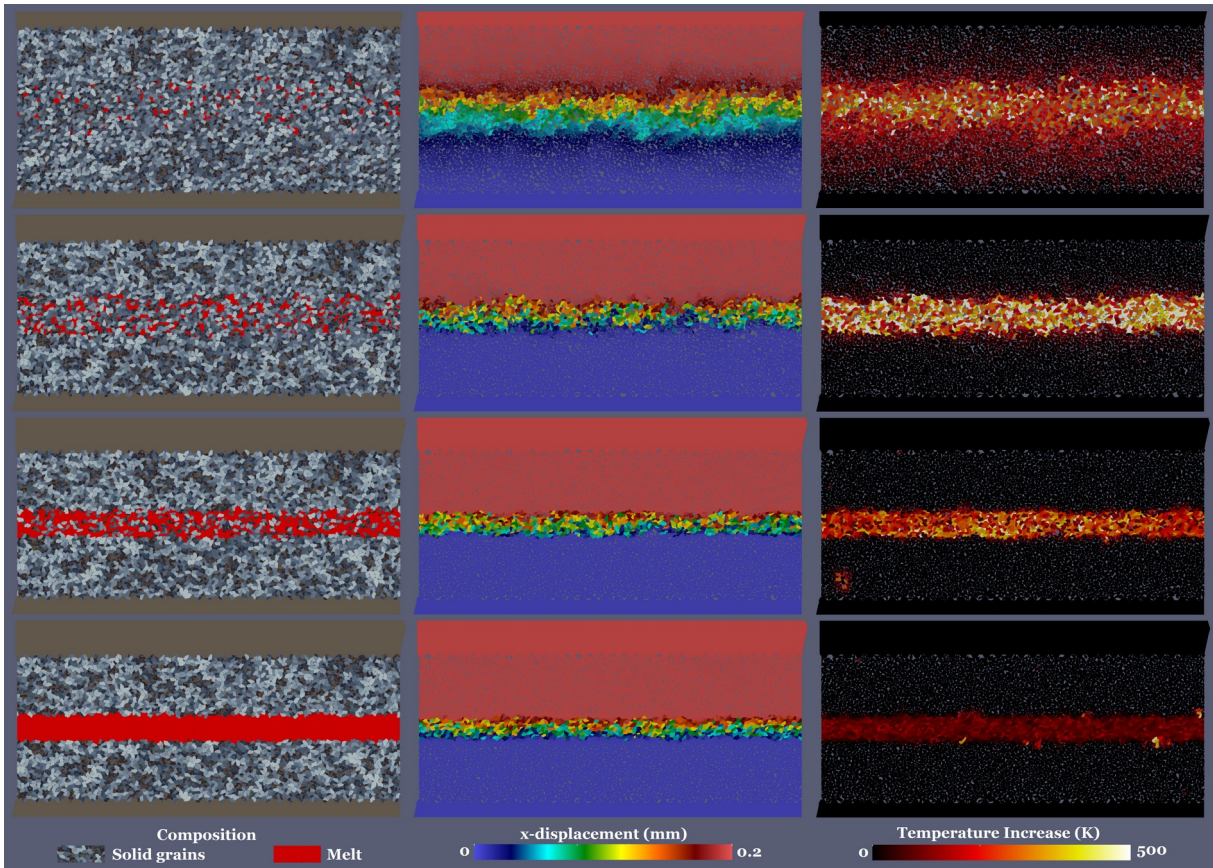
371 proportion of melt tends to reduce the intensity of the initial friction peak (meaning that it
 372 progressively suppresses dilatancy), and to reduce the steady-state friction coefficient (from
 373 0.457 for 10% of melt to 0.082 for 100% of melt). It also stabilizes the friction signal by
 374 reducing the intensity of its fluctuations.
 375



376
 377 *Fig.10. Friction time-series for four different fractions of melt in the central layer; thin lines: raw*
 378 *numerical data; bold lines: moving average*

379
 380 Figure 11 provides the spatial distributions of the molten grains, the field of horizontal
 381 displacements, and the field of temperature increases (in the adiabatic case) for the same four
 382 cases. This temperature increase includes both the energy coming from the frictional contacts
 383 between solid grains and the viscous dissipation in soft grains. For low melt proportion, some
 384 molten grains are transported in the transversal direction during shearing, while this is not
 385 observed for the fully molten layer. Likewise, the mobilized thickness over which a certain
 386 amount of shear is accommodated is much larger at low melt fractions (i.e. close to the dry
 387 case, at $\phi_m=10\%$, for example), but is fully localized in the case of a fully molten layer (ϕ_m
 388 $=100\%$). This trend, combined with the friction curves (Figure 10), leads to a surprising result

389 in terms of heat generation. As shown in Figure 11 (right-panel), an intermediate value of ϕ_m
 390 ($\sim 30\%$) maximizes the adiabatic temperature increase in the grains. For lower melt fractions
 391 (e.g. $\phi_m=10\%$) the heat creation is less localized, while it is more localized but less intense for
 392 larger melt fractions (e.g. $\phi_m=60\%$), owing to a lower apparent friction coefficient.
 393

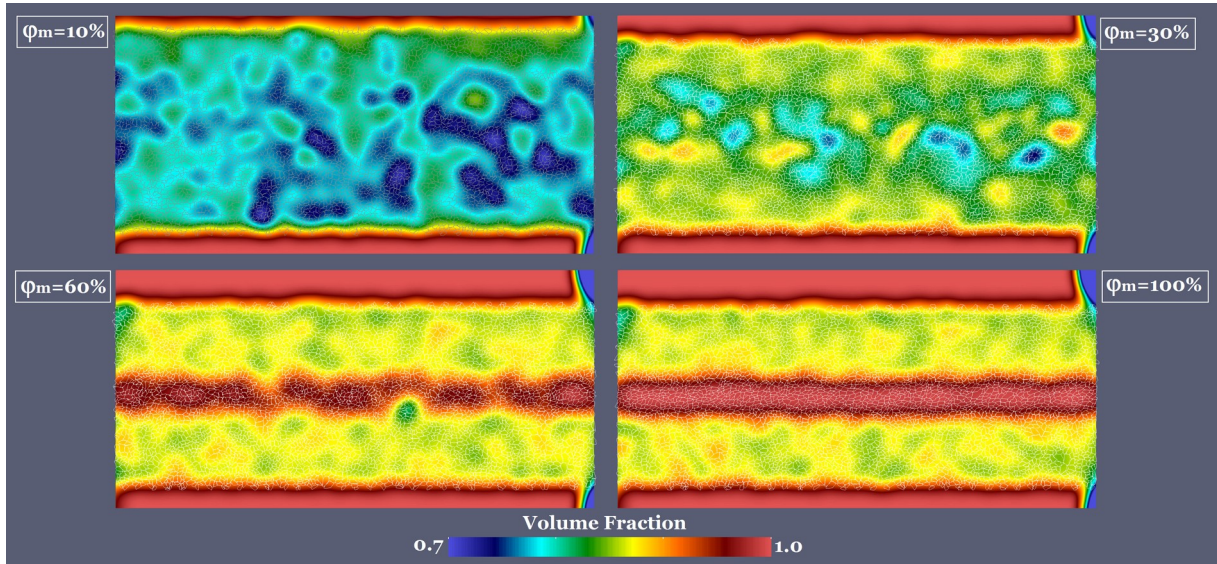


394
 395 *Fig.11. Views of sliding faults with partial melting in the central layer after 200 μm of sliding distance;*
 396 *Left-panel: distribution of molten grains, in red; Central panel: horizontal displacement of each*
 397 *grain; Right-panel: Temperature increase in each grain (adiabatic case). Top to bottom: 10%, 30%;*
 398 *60%; 100% of melt in the central layer*

399
 400 Figure 12 provides the fields of volume fraction (i.e. proportion of the fault volume occupied
 401 by the solid and the molten grains) for the same cases. The case with 10% of melt shows a
 402 very similar behaviour to a purely dry gouge, i.e. shearing and dilation in a broad shear band.

403 When the melt fraction is increased to 30%, dilation takes place in a less broad area. For
404 higher melt fractions, no dilation takes place in the granular part and porosity is close to zero
405 in the melt layer.

406



407

408 *Fig.12. Volume fraction in sliding faults with partial melting in the central layer after 200 μm of*
409 *sliding distance*

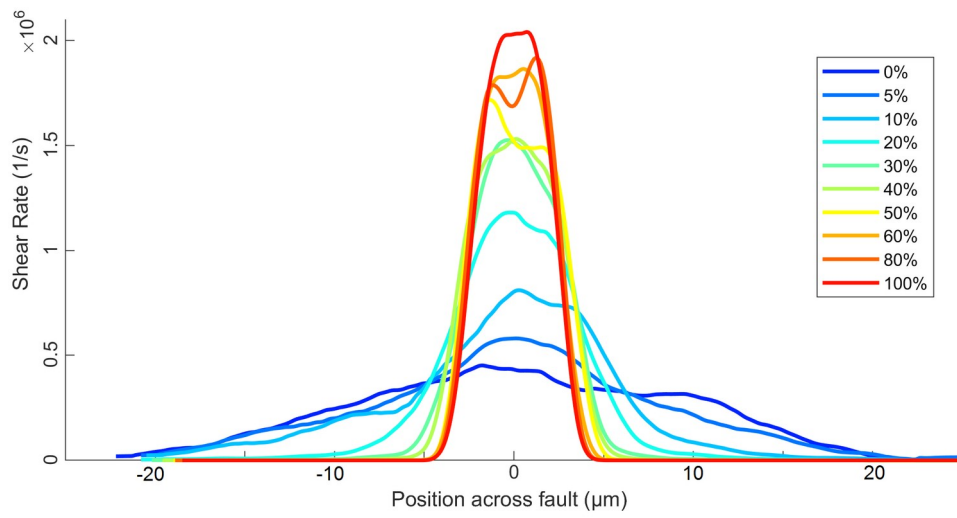
410

411 Shear rate profiles across the fault (averaged on horizontal slices) are provided for different
412 melt fractions in Figure 13, illustrating the progressive localization promoted by the presence
413 of melt. The accommodation zone ranges from about 40 μm for $\phi_m=0\%$ (purely granular
414 localization) to about 8 μm for $\phi_m=100\%$ (shear restricted to the liquid layer). In this latest
415 case, the steady state apparent friction coefficient provided in Figure 10 combined with the
416 shear rate averaged on the melt layer leads to an equivalent viscosity of the simulated melt
417 layer $\eta_m=10.0$ Pa.s. This value is close to the lower range of values measured on carbonated
418 rocks, see for example (Kono et al., 2014).

419

420

421



422

423

Fig.13. Shear rate across the fault for different values of the melt proportion

424

425

426

427 V. DISCUSSION

428 *a. Friction and rheology*

429 Based on the simulations, steady-state fault friction can be interpreted following:

$$F = \frac{\dot{W}_c + \dot{W}_v}{\sigma_n \cdot \Delta V} \quad (3)$$

430 where ΔV is the applied sliding velocity; \dot{W}_c is the average rate of mechanical work dissipated
431 by contacts between solid grains and \dot{W}_v is the average rate of mechanical work dissipated by
432 the viscosity in molten grains. These two work rates can be extracted from a given simulation
433 by techniques analogous to those used to compute adiabatic temperature increase in each
434 grain in Section III. Following the logic presented in (Mollon 2019), we can compute F_c and
435 F_v , the apparent friction coefficients related to the Coulomb and viscous contributions acting
436 in the gouge layer, respectively:

$$F_c = \frac{\dot{W}_c}{\sigma_n \cdot \Delta V} \quad (4)$$

$$F_v = \frac{\dot{W}_v}{\sigma_n \cdot \Delta V} \quad (5)$$

437 These contributions are plotted as a function of the melt fraction φ_m for the whole numerical
438 campaign (Figure 14). Two end-members can be identified: (i) the case $\varphi_m=0\%$, which
439 strictly corresponds to Coulomb friction, with a total friction coefficient of 0.460; and (ii) the
440 case $\varphi_m=100\%$, which corresponds to purely viscous friction with a total friction coefficient
441 of 0.082. We observe that numerical results close to this second end-member are in good
442 accordance with the well-known Einstein formula (Coussot and Ancy, 1999), which is valid
443 for highly diluted suspensions of rigid grains in a Newtonian fluid. Adapted to the notations
444 of the present work, this formula follows:

$$F = F_v \cdot (1 + 2.5(1 - \varphi_m)) \quad (6)$$

445

446 For melt fractions below 70-80%, however, results logically deviate from this simple law (Eq.
447 (6)) because interparticle dry friction comes into play.

448

449 It is instructive to compare the simulation results to a simple linear mixing law that would
450 state that the contribution of each phase be proportional to its volume fraction in the mixture.

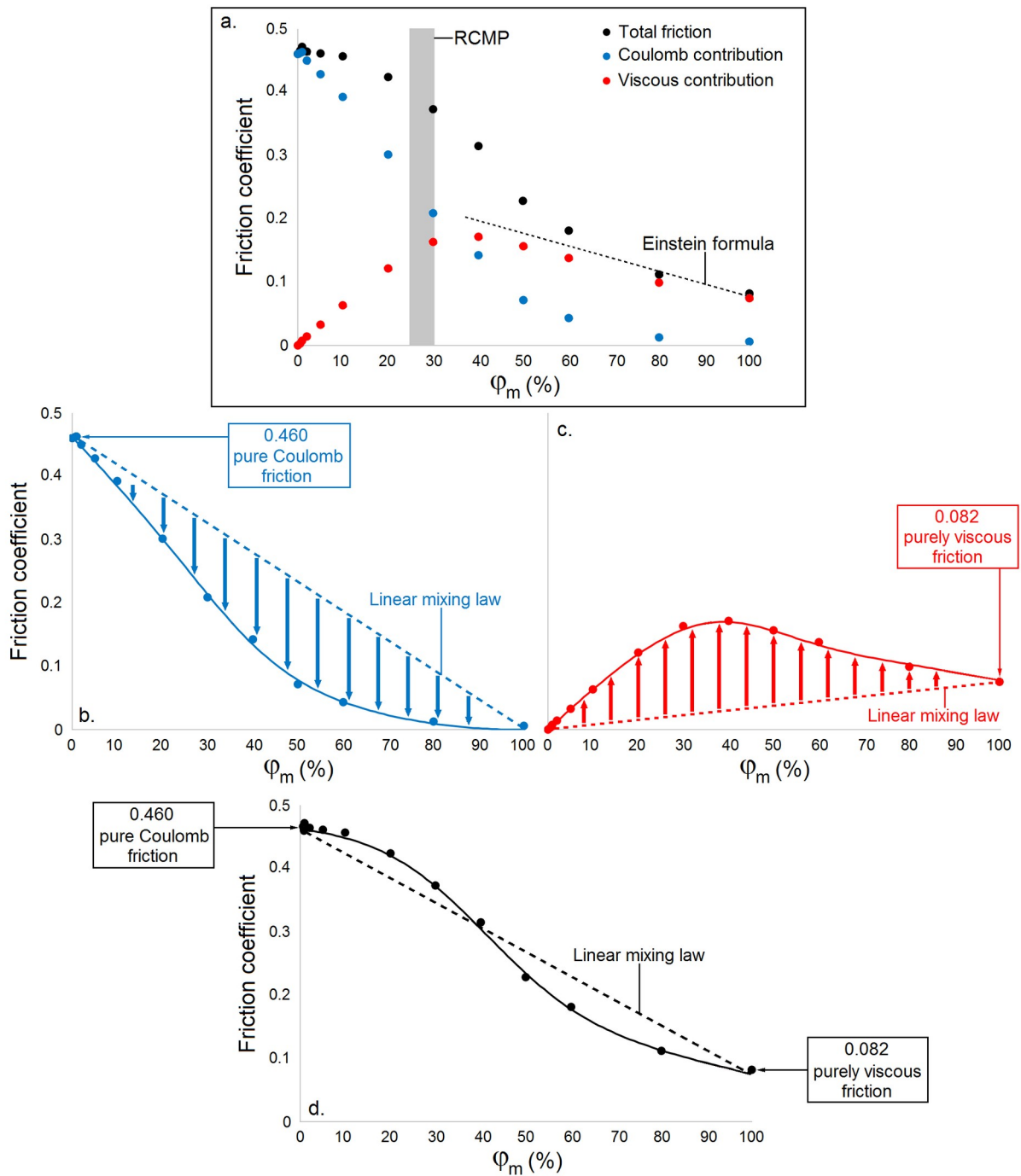
451 It would thus give:

$$F_c = 0.460 \cdot (1 - \phi_m) \quad (7)$$

$$F_v = 0.082 \cdot \phi_m \quad (8)$$

452 Although correct at the two end-members, this simple law does not appear to fit
453 correctly the data (Figure 14b-d). The linear mixing model overestimates the contribution of
454 interparticle friction in the response of the mixture to shearing (Figure 14b). As the proportion
455 of molten grains increases, the remaining dry grains appear to dissipate less energy than their
456 share. This is especially the case when reaching melt contents around 50%, for which the
457 contribution of dry grains to friction becomes very low while they still are rather numerous in
458 the partially molten layer. In addition to reducing the number of solid grains, melting also
459 seems to reduce the frictional efficiency of grain contacts.

460



461

462 *Fig. 14. Influence of partial melting on friction coefficient; a. Numerical results; b. Coulomb*

463 *contribution to friction; c. Viscous contribution; d. Total friction; Dots indicate simulation data, solid*

464 *lines are just guides to the eye, dotted lines in b., c. and d. are a simple linear mixing law*

465

466 In contrast, the linear mixing model underestimates the energy dissipated by viscous

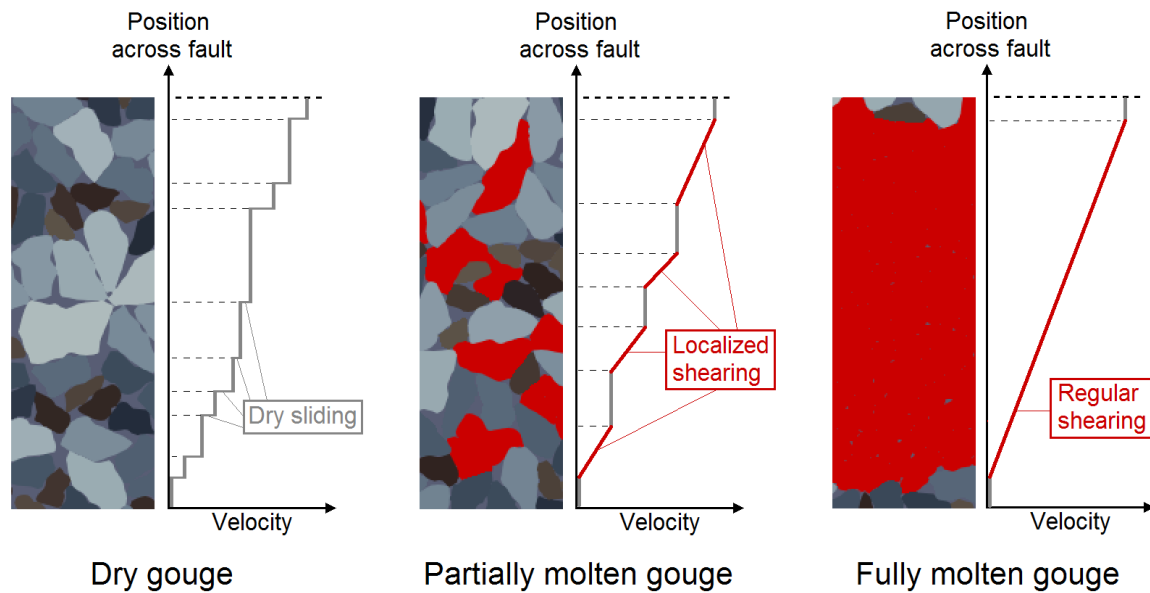
467 deformation of the molten grains (Figure 14c). For melt fractions from 20 to 50%, where the

468 amount of molten grains is still rather low, viscous dissipation contributes to the overall
469 friction coefficient close to 0.15-0.18. This is twice larger than the friction obtained for a fully
470 molten layer. The interplay between rigid grains and melt leads to local shear rates which are
471 much larger than the average one (Figure 15). When adding both contributions to friction, an
472 interesting deviation from the linear mixing model appears (Figure 14d). Instead of a linear
473 decrease of friction with the increase of φ_m , numerical results suggest a sigmoid shape, with a
474 more sudden drop for intermediate values of φ_m (~30-60%). We note that this result is in
475 agreement with values of the Rheological Critical Melt Percentage (i.e. the melt fraction
476 above which a cristal-bearing magma departs from its solid state and starts behaving as a
477 viscoplastic fluid), estimated by Arzi (1978) to be of the order of 25-30% (Fig14a). The
478 agreement extends to the general shape of the weakening curve beyond 30%, which is
479 reported experimentally in Costa et al. (2009) to approach a decreasing exponential. It should
480 be noted, however, that such results were obtained in a rather different context (i.e. slow
481 shearing of bulk crystalline rock deformed at very low strain rates, for volcanology
482 applications). Nevertheless, the behavior obtained in our simulations is likely to promote a
483 slightly more delayed but also more prompt fault weakening.

484

485

486



487

488 *Fig.15. Sketch of the accommodation modes for dry, partially molten, and fully molten gouge (highly*
 489 *simplified representation disregarding rotations and vertical motions of grains)*

490

491 ***b. From numerical modeling to experiments: the concept of flash heating and***
 492 ***frictional melting***

493 Simulation results in intact gouge prior to melting are in good agreement with several
 494 experimental and theoretical studies describing shear localization in a thin and compacted
 495 gouge layer (Sone and Shimamoto, 2009; Rice et al., 2014; Platt et al., 2014). However, this
 496 study questions the way seismic faults subjected to flash heating and frictional melting are
 497 conceptualized in many theoretical models. Most of these models indeed rely on the concept
 498 of “asperity”, seen as a geometrical feature that bears a very large proportion of the normal
 499 load and therefore concentrates heat creation. However, all experimental evidences point
 500 towards the fact that bare rock surfaces are almost immediately separated by a layer of fault
 501 gouge because of the degradation of the sliding surfaces (Aubry et al., 2018; Aubry et al.,
 502 2020). The size of the asperities is closely related to confining pressure and the average
 503 contact lifetime on the sliding interface (Dieterich and Kilgore, 1994; Rice, 2006; Aubry et
 504 al., 2020). Based on an analogy with state evolution distance in RSF models, asperity sizes

505 proposed in Rice (2006) are of the order of 5 μm , while slip localization thickness in well-
506 established gouge is postulated in the same study to be in the range 10-20 μm , up to 100-300
507 μm in principal natural slip zone. Recent laboratory earthquakes experiments showed that the
508 newly-created gouge layer thickness is in the order of 10 μm , while post-mortem temperature
509 estimates by carbon deposition techniques point towards asperity sizes of the order of 100 μm
510 (Aubry et al., 2018; Aubry et al., 2020).

511 In the case of granular and soft materials, temperature heterogeneities between grains
512 (enhanced by extremely localized heat creation at particle contacts but attenuated by heat
513 diffusion) seems to lead to melting in the areas where the strain rate is the largest. This partial
514 melting would first concern the grains with the highest temperatures and the lowest melting
515 points, but would not immediately lead to a large reduction in friction. Conversely, when the
516 melt fraction increases, friction drop is moderate and the strain rate in the molten zone
517 increases (Figure 13). In that specific case, the onset of melting does not act as a self-limiting
518 phenomenon as often proposed, but would appear to have a positive feedback (Figure 11,
519 right-hand panel). Under the assumptions of the present study, we can thus expect fault
520 weakening to be more sudden than expected in most models. This process eventually stops
521 when partial melting reaches values corresponding to a much larger fault weakening.
522 Depending on normal stress and sliding velocity, a balance may be reached between heat
523 creation and heat diffusion when the deformation is entirely localized.

524 In contrast with some theoretical models (Platt et al., 2014; Rice et al., 2014), our model
525 does not invoke rate-dependent gouge dilatancy or rate-strengthening friction in order to
526 prevent localization. When completely established, strain localization might be a self-limiting
527 phenomenon because of a progressive shift from granular (prone to localization) to viscous
528 (prone to de-localization) friction as the melt fraction increases in the interface.

529

530 *c. Further developments and requirements for a dynamic friction model*

531 The numerical framework presented in the present study has several limitations: (i) the
532 reported simulations rely on a simple assumption in terms of melt distribution in the gouge
533 layer (i.e. homogeneous distribution in a certain central layer of the gouge), (ii) the numerical
534 model can only deal with heat creation and diffusion in an indirect way (relying on a second
535 pass on stored results with back-calibrated contact thermal conductivities), and does not
536 account for the dependency of melt viscosity on temperature, (iii) it only deals with steady-
537 state simulations since it does not simulate the melting process explicitly (it can consider the
538 initial presence of melt in a simulation, but not the change of phase), (iv) it leads to very long
539 simulations which prevent extensive numerical campaigns, and (v) it is extremely local and
540 cannot be strongly coupled with the overall dynamics of the seismic sliding of a whole fault.

541 A (semi-)analytical model seems necessary to go beyond these limitations. This model
542 will have to take advantage of the results gathered in the numerical campaign described in the
543 present paper, in order to predict the friction coefficient and the shear rate profile at any time,
544 based only on the distribution of the melt fraction in the interface. It will also have to deal
545 with heat production and diffusion (between grains and in the surrounding medium), with
546 melting enthalpy, with the dependence of the fluid viscosity with temperature, with the
547 variations in space and time of the sliding velocity along the fault, and with the reduction of
548 the thermal conductivity of the sheared gouge.

549 An important point will be the necessity to account for the mineral composition of the
550 pulverized rock composing the gouge, since each grain made of a different mineral is
551 expected to have a different melting point (Aubry et al., 2018). Finally, it will be necessary to
552 connect it with the inertial effects in the surrounding medium. Eventually, we can expect the
553 implementation of a temporal dimension in a more general semi-analytical model
554 implemented at each discrete point of a fault surface. Another issue regarding comparisons

555 with experiments is the model ability to predict the transient fault strengthening which is
556 sometimes observed in high-velocity shear experiments before the establishment of a
557 pervasive layer of molten rock (Hirose and Shimamoto, 2005). This strengthening is
558 attributed to viscous resistance of the very first patches of melt, submitted to very large strain
559 rates, before their merging and heating reduces both shear rate and viscosity and eventually
560 leads to fault weakening.

561

562 **VII. CONCLUSION**

563 Two simulation campaigns were undertaken in order to investigate shear-heating-
564 related phenomena at the scale of granular fault gouge. The first one investigated the
565 influence of the fault thickness during the first stages of the seismic sliding (i.e. before the
566 first appearance of melt), while the second focused on the influence of the proportion of
567 molten grains in the central area of a gouge layer. We found that granular gouges naturally
568 tend to localize shearing in a narrow area, corresponding to a few tens of the average grain
569 diameter. Instantaneous strain rate profiles were even found to be thinner (e.g. about ten
570 grains diameters), but switching rapidly from one active site to another during sliding. The
571 temperature distribution in a given layer of the gouge was nearly Gaussian, with standard
572 deviations of a few Kelvins. It was observed that, upon shearing, the bulk thermal
573 conductivity of the gouge was divided by a factor 2.5, because of the dilatancy-induced loss
574 of a large number of mechanical contacts.

575

576 The introduction of molten grains in the central area of the fault gouge led to a reduction in
577 friction. This friction reduction is not proportional to the amount of melt, but occurs more
578 suddenly, following a sigmoid-like weakening phenomenology. The respective contributions
579 of the solid and molten grains in the resistance to shear showed that solid grains resist less to

580 shearing than their share (because melt lubricates their contacts) but molten grains resist more
581 than theirs (because they experience larger local strain rates when trapped between solid
582 grains). Melt presence leads to a more intense localization of the shearing, and thus to fast
583 fault weakening. This positive feedback stops when the amount of melt gives to the interface
584 a sufficiently viscous character. The requirements for a future friction law accounting for all
585 these phenomena were listed, in the perspective of introducing such a law in semi-analytical
586 dynamic simulations of seismic sliding.

587

588

589

590 **DISCLOSURE**

591 The authors acknowledge that this study contains original material, as a result of a purely
592 academic study without any kind of private funding or conflict of interest. Its publication has
593 been approved tacitly by the responsible authorities at the institutes where the work has been
594 carried out.

595

596 **DATA AVAILABILITY STATEMENT**

597 All simulations were performed with the open-source software MELODY version 3.94 (DOI:
598 10.5281/zenodo.4305614) developed by the first author and described in Mollon (2018).
599 Simulation data can be found at: Mollon, Guilhem (2020), “Simulating melting in seismic
600 fault gouge”, Mendeley Data, V1, doi: 10.17632/n8bwrtzsjd.1

601

602

603

604

605

606

607

608

609

610

611

612

613

614

615

616

617 **REFERENCES**

- 618 Arzi, A. (1978), Critical phenomena in the rheology of partially melted rocks, *Tectonophysics*,
619 44, 173-184
620
- 621 Aubry, J., Passelègue, F. X., Deldicque, D., Girault, F., Marty, S., Lahfid, A., Bhat, H. S.,
622 Escartin, J., and Schubnel, A. (2018), Frictional heating processes and energy budget during
623 laboratory earthquakes, *Geophysical Research Letters*, 45, 12, 274-282
624
- 625 Aubry, J., Passelègue, F. X., Escartin, J., Gasc, J., Deldicque, D., and Schubnel, A. (2020),
626 Fault stability across the seismogenic zone, *Journal of Geophysical Research: Solid Earth*,
627 125(8)
628
- 629 Bizzarri, A. (2009), Can flash heating of asperity contacts prevent melting?, *Geophysical*
630 *Research Letters*, 36, L11304
631
- 632 Costa, A., Caricchi, L., and Bagdassarov, N. (2009), A model for the rheology of particle-
633 bearing suspensions and partially molten rocks, *Geochemistry, Geophysics, Geosystems*, 10(3)
634
- 635 Coussot, P., and Ancey, C. (1999), Rheophysical classification of concentrated suspensions
636 and granular pastes, *Physical Review E*, 59, 4445-4457
637
- 638 Cundall, P.A., Strack, O.D.L. (1979), A discrete numerical model for granular Assemblies,
639 *Geotechnique*, 29, 47-65
640
- 641 Di Toro, G., Goldsby, D. L., and Tullis, T. E. (2004), Friction falls towards zeros in quartz
642 rock as slip velocity approaches seismic rates, *Nature*, 427(6973), 436-439
643
- 644 Di Toro, G., Hirose, T., Nielsen, S., Pennacchioni, G., and Shimamoto, T. (2006), Natural and
645 Experimental Evidence of Melt Lubrication of Faults During Earthquakes, *Science* 311(1),
646 647-649
647
- 648 Dieterich J., H., and Kilgore, B. D. (1994), Direct observation of frictional contacts: new
649 insights for state-dependent properties, *Pure and Applied Geophysics*, 143(1-3), 283-302
650
- 651 Forterre, Y., and Pouliquen, O. (2008), Flow of dense granular media, *Annual Review of Fluid*
652 *Mechanics*, 40, 1-24
653
- 654 Goldsby, D. L., and Tullis, T. E., (2002), Low frictional strength of quartz rocks at subseismic
655 slip rate, *Geophysical Research Letters*, 29(17), 1844
656
- 657 Goldsby, D. L., and Tullis, T. E. (2011), Flash heating leads to low frictional strength of
658 crustal rocks at earthquake slip rates, *Science*, 334(6053), 216-218
659
- 660 Guo, Y., and Morgan, J. K. (2007), Fault gouge evolution and its dependence on normal stress
661 and rock strength – Results of discrete element simulations: Gouge zone properties, *Journal*
662 *of Geophysical Research*, 112, B10403
663
- 664 Han, R., Shimamoto, T., Hirose, T., Ree, J. H., and Ando, J. (2007), Ultralow friction of
665 carbonate faults caused by thermal decomposition, *Science*, 316, 7-12

666
667 Han, R., Hirose, T., and Shimamoto, T. (2010), Strong velocity weakening and powder
668 lubrication of simulated carbonate faults at seismic slip rates, *Journal of Geophysical*
669 *Research: Solid Earth*, 115(3)
670
671 Hirose, T., and Shimamoto, T. (2005), Growth of molten zone as a mechanism of slip
672 weakening of simulated faults in gabbro during frictional melting, *Journal of Geophysical*
673 *Research: Solid Earth*, 110(5), 1-18
674
675 Iordanoff, I., Fillot, N., and Berthier, Y. (2005), Numerical study of a thin layer of cohesive
676 particles under plane shearing, *Powder Technology*, 159, 46-54
677
678 Kono, Y., Kenney-Benson, C., Hummer, D., Ohfuji, H., Park, C., Shen, G., Wang, Y.,
679 Kavner, A., and Manning, C. E. (2014), Ultralow viscosity of carbonate melts at high
680 pressures, *Nature Communications*, 5, 5091
681
682 Madhusudana, C. V., and Ling, F. F. (1995), Thermal Contact Conductance, Springer, 1996
683 edition, 184p.
684
685 MiDi (2004), On dense granular flows, *The European Physical Journal E*, 14, 341-365
686
687 Mollon, G., and Zhao, J. (2012), Fourier-Voronoi-based generation of realistic samples for
688 discrete modelling of granular materials, *Granular Matter*, 14, 621-638
689
690 Mollon, G. (2015), A numerical framework for discrete modelling of friction and wear using
691 Voronoi polyhedrons, *Tribology International*, 90, 343-355
692
693 Mollon, G. (2018), A unified numerical framework for rigid and compliant granular materials,
694 *Computational Particle Mechanics*, 5, 517-527
695
696 Mollon, G. (2019), Solid flow regimes in dry sliding contacts, *Tribology Letters*, 67:120
697
698 Mollon, G., Quacquarelli, A., Andò, E., and Viggiani, G. (2020), Can friction replace
699 roughness in the numerical simulation of granular materials?, *Granular Matter*, 22(42)
700
701 Muto, J., Nakatani, T., Nishikawa, O., and Nagahama, H. (2015), Fractal particle size
702 distribution of pulverized fault rocks as a function of distance from the fault core,
703 *Geophysical Research Letters*, 42, 3811-3819
704
705 Nielsen, S., Di Toro, G., Hirose, T., and Shimamoto, T. (2008), Frictional melt and seismic
706 slip, *Journal of Geophysical Research: Solid Earth*, 113(1), 1-20
707
708 Passelègue, F. X., Schubnel, A., Nielsen, S., Bhat, H. S., Deldicque, D., and Madariaga, R.
709 (2016), Dynamic rupture processes inferred from laboratory microearthquakes, *Journal of*
710 *Geophysical Research: Solid Earth*, 121, 4343-4365
711
712 Platt, J. D., Rudnicki, J. W., and Rice, J. R. (2014), Stability and localization of rapid shear in
713 fluid-saturated fault gouge: 2. Localized zone width and strength evolution, *Journal of*
714 *Geophysical Research: Solid Earth*, 119, 4334-4359
715

716 Reches, Z., and Lockner, D. A. (2010), Fault weakening and earthquake instability by powder
717 lubrication, *Nature*, 467(7314), 452-455
718
719 Renouf, M., Cao, H.-P., and Nhu, V.-H. (2011), Multiphysical modeling of third-body
720 rheology, *Tribology International*, 44, 417-425
721
722 Rice, J.R. (2006), Heating and weakening of faults during earthquake slip, *Journal of*
723 *Geophysical Research: Solid Earth*, 111(5), 1-29
724
725 Rice, J.R., Rudnicki, J.W., and Platt, J.D. (2014), Stability and localization of rapid shear in
726 fluid-saturated fault gouge: 1. Linearized stability analysis, *Journal of Geophysical Research:*
727 *Solid Earth*, 119, 4311-4333
728
729 Sone, H., and Shimamoto, T. (2009), Frictional resistance of fault during accelerating and
730 decelerating earthquake slip, *Nature Geoscience*, 2, 750-708
731
732 Sulem, J., Famin, V., and Noda, H. (2009), Thermal decomposition of carbonates in fault
733 zones: slip-weakening and temperature-limiting effects, *Journal of Geophysical Research*,
734 114(B6), 1-14
735
736 Torsedillas, A., Peters, J. F., and Gardiner, B. S. (2004), Shear band evolution and
737 accumulated microstructural development in Cosserat media, *International Journal of*
738 *Numerical and Analytical Methods in Geomechanics*, 28, 981-1010
739
740 Vosteen, H.-D., and Schellschmidt, R. (2003), Influence of temperature on thermal
741 conductivity, thermal capacity and thermal diffusivity for different types of rock, *Phys. Chem.*
742 *Earth*, 28, 499-509
743
744 Wibberley, C. A., and Shimamoto, T. (2005), Earthquake slip weakening and asperities
745 explained by thermal pressurization, *Nature*, 436 (7051): 689-692
746
747